Modulation of high-energy electrons with a nanopore matter lens

Guangyi Huang,* Wenhao He,* Xian Li, and Changlin Zheng†
State Key Laboratory of Surface Physics and Department of Physics, Fudan University, Shanghai 200438, China

(Received 31 December 2023; accepted 3 June 2026; published 26 June 2026)

We demonstrate the modulation of high-energy electrons using a nanosized pore in solid as a strong electrostatic lens. The inner Coulomb potential of matter decreases rapidly from the edge of the pore toward the center, creating a strong electric field on the order of 10 GV/m. This electric field strongly modulates the phase of the incident electron beam and deflects the beam as a defocusing lens. We measure the strength of the electric field by combining electron holography with quantitative scanning transmission electron microscopy. We also observe changes in the transmitted probe through the nanopore using electron confocal imaging. The shrinking electron Airy patterns on the detector plane indicate that the exit probe's convergent angle increases under the deflection of the nanolens. This behavior corresponds to an effective concave lensing effect that cannot be achieved with rotationally symmetric electromagnetic fields in vacuum due to fundamental constraints imposed by the governing field equation. This demonstration of electron matter lensing shows the potential to manipulate high-energy electrons at the nanometer scale, expanding conventional electromagnetic lensing into nanoelectron optics.

DOI: 10.1103/2mgp-xgv1

I. INTRODUCTION

Transmission electron microscopy (TEM) is a leading scientific instrument used to study condensed matter at the nanoscale and atomic scale [1–4]. In TEM, electrons are accelerated to tens or hundreds of kilo-electron-volts (keV), resulting in an extremely short wavelength of only a few picometers. Since the wavelength is much shorter than the atomic spacing in solids, high-energy electrons are extensively used to analyze the crystallographic structure of solids. In comparison to x-rays and thermal neutrons [5,6], electrons have a unique advantage: They can produce extremely high-resolution real-space images through electromagnetic lensing, while electric or magnetic fields can readily alter the trajectories of electrons [7]. Therefore, TEM can offer both averaged crystallographic structure in diffraction space and localized structural changes in real space. The latest generation of TEM has achieved a spatial resolution surpassing 0.5 Å [8,9], allowing for the imaging and spectroscopy of individual atoms [10–12], the detection of atomic fields and charge transfers between bonded atoms [13–17], and even the observation of single-atom magnetization [18].

Despite the continuous improvement of resolution in TEM [19–21], the fundamental architecture of the TEM has remained unchanged since its invention in 1933 [22]. High-energy electrons are primarily focused using magnetic lenses, which produce a magnetic field by a set of winding coils carrying large electric currents [7,23]. The strength of the magnetic field generated is limited to about 2 T. This results in a finite flux density and restricts the focusing capability for high-velocity electrons (∼0.8 speed of light in vacuum at 300 keV). The focal length of the magnetic lens in TEM is typically in the millimeters range. Additionally, the rotationally symmetric fields of conventional TEM objective lenses introduce severe positive third-order spherical aberration (Cs), and the Cs coefficient is in the same order as the focal length, significantly limiting the achievable resolution in an uncorrected TEM [24]. Unlike visible-light optical systems, there is also a lack of concave magnetic lenses to directly compensate for the positive spherical aberrations. Current aberration correctors use multiple poles to generate a nonrotational magnetic field for cancelling out spherical aberrations [25]. To achieve atomic imaging with sufficient magnification, it is necessary to integrate multistage magnetic lenses and correctors, further increasing the complexity and volume of modern electron microscopes.

Recently, different types of electron lenses have been developed to improve the focusing power for high-energy electrons. A discharge-capillary active plasma lens can achieve field gradients of over 3 kT/m [26], and a plasma wakefield lens can further reach 1 MT/m [27]. Despite this, these applications are currently limited to particle accelerators. Electron manipulation and lensing based on free electron quantum optics have also been developed [28], coupling free electrons with intense lasers in a vacuum or through nanostructures [29,30]. For instance, direct diffracting and phasing of electrons using the ponderomotive potential generated in a strong light field has been demonstrated [30] and developed as a phase plate for enhancing the contrast for biological electron imaging [31]. Theoretical studies also reveal the electron lensing properties of the ponderomotive potential generated by Bessel and Laguerre-Gaussian beams and the future applications for spherical correction in TEM

*These authors contributed equally to this work.
†Contact author: zcl@fudan.edu.cn

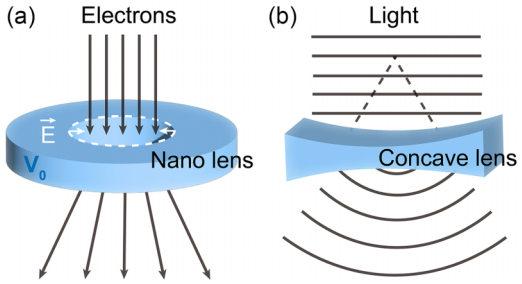

FIG. 1. (a) Illustration of high-energy electrons transmitting through a subnanometer pore in matter, deflecting due to the strong local electric field, analogous to (b) light deflected by a concave lens.

[32]. However, engineering these lenses remains a significant challenge due to the requirement of electrons precisely interacting with a highly intense laser. A laser-driven, dielectric laser accelerator-based electrodynamic lens has also shown promise in focusing high-energy electrons over short distances [33]. However, it only applies to pulsed electrons and not continuing beams. Therefore, it is crucial to continue developing varieties of electron lenses.

In this work, we explore the potential of modulating and lensing free electrons by utilizing the inherent Coulomb potential of matter at the nanometer scale. Electron phase modulation using the internal Coulomb or magnetic potential of materials has been developed and applied for enhancing phase contrast in TEM. For example, Boersch [34,35], Zernike [36], and Volta-type phase plates [37], as well as tunable Ampere phase plates [38], have been developed to improve contrast in low Z materials (particularly biological samples). The phase modulation by utilizing matter Coulomb or magnetic potential of matter has also been applied for correcting aberrations in TEM or generating singular electron beams like Bessel or vortex beams [39–48]. However, the interaction range has remained in the micrometer scale. In this work, we further push the field constraint into the subnanometer range, enhancing the field strength and phase gradient by up to 3 orders of magnitude. This opens the possibility of extending conventional electromagnetic lensing into nanoscale electron optics.

II. METHOD AND EXPERIMENTAL RESULTS

The basic principle of nanoscale electron lensing is illustrated in Fig. 1(a). When high-energy electrons transmit through a nanosized pore embedded in amorphous carbon, they will be deflected by the inner electric field within the pore, similar to light deflected by a concave lens [Fig. 1(b)].

The preparation of the nanopore, imaging of electrostatic potential distributions within the nanopore lens, and observation of electron deflecting effects were conducted using a double aberration-corrected field-emission S/TEM (Thermo Fisher Themis ZS/TEM) operating at 300 kV. The microscope is equipped with a CEOS SCORR probe and a CETCOR image corrector, and a Gatan 1066 imaging filter (GIF). To prepare a subnanosized pore, a high-current electron probe (200 pA) was incident into an amorphous carbon to sputter the carbon atoms for 30 s, as shown in Fig. 2(a). The full width at half maximum (FWHM) of the high-angle annular dark-field

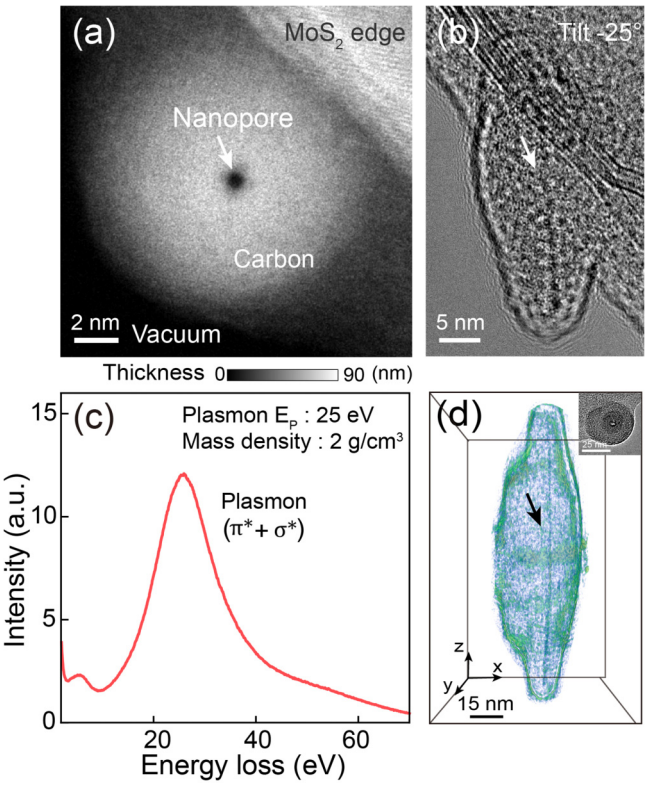

FIG. 2. Morphology and structure of nanopore lens. (a) Quantitative STEM thickness mapping of the amorphous carbon and the subnanometer pore. (b) BF-TEM image of the nanopore imaged with a 25° tilt. The dark line reveals the tubular hole in the carbon. (c) The low-energy EEL spectrum of the amorphous carbon shows the plasmon excitation peaking at 25.3 eV. (d) 3D reconstruction of BF-TEM tomography of a similar nanopore and the surrounding area. Inserted: TEM image at 0°.

scanning transmission electron microscopy (HAADF-STEM) intensity line profile across the nanopore is approximately 0.8 nm, revealing an extremely small pore. The details of the pregrowth of amorphous carbon along the edge of monolayer MoS_2 are given in Supplemental Material [49].

Since the HAADF-STEM image only provides a two-dimensional projection of the object, we used quantitative STEM to measure the carbon thickness and the pore length along the beam direction [50–53]. This was performed by normalizing the scattered electron density falling on the HAADF detector to the total incident beam. The resulting fractional intensity was then compared to a precalculated dataset as a function of carbon thickness. For electron dynamical scattering calculation with a multislice approach, we constructed the amorphous structure of carbon using an average mass density of 2.0 g/cm^3, which is extracted from the peak location of plasmon excitation at 25.3 eV in electron energy loss spectroscopy (EELS) [Fig. 2(c)]. The plasmon loss in EELS provides information about the valence electron density and, consequently, the mass density of the carbon.

The quantitative STEM measurement shows that the amorphous carbon film surrounding the pore has an average thickness of 69 ± 1 nm, suggesting that the carbon has grown columnar. Despite the lateral size of the entire carbon showing

only ∼10 nm from the top view, the nanopore forms a long tube with an aspect ratio of ∼90. To further confirm this, the sample was tilted by 25° and reimaged in bright field (BF-TEM) mode, as shown in Fig. 2(b). The BF-TEM image confirms the presence of a nanosized pore (dark contrast) with a large aspect ratio that penetrates through the carbon. In addition, a BF-electron tomography experiment was conducted on a similar sample to reconstruct the three-dimensional (3D) morphology of the nanopore. The reconstructed 3D morphology in Fig. 2(d) depicts a long nanotube embedded in the carbon.

With respect to the vacuum energy level, each isolated carbon atom has a positive Coulomb potential due to the presence of a positively charged nucleus screened by the negatively charged electrons. When these carbon atoms bond into a solid, the solid exhibits a positive mean inner Coulomb potential. In the case of nanopores embedded, the mean inner Coulomb potential is expected to rapidly decrease from the edge to the vacuum, resulting in a strong local electrostatic field. We used off-axis electron holography with parallel beam illumination to map the Coulomb potential and the electric field. The holography experiment was performed in high-resolution mode, with electron biprism voltage set to 300 V. The generated holographic interference fringe spacing was measured to 72 pm, with an average fringe contrast of 25%. Phase reconstruction was performed using the standard Fourier transform method, and a circular virtual aperture ($r = 3.21\,\mathrm{nm}^{-1}$) was applied to select the sideband in the diffractogram.

Figure 3(a) shows the unwrapped phase image of the nanopore and its surrounding carbon reconstructed from an electron hologram. A phase line profile across the center of the nanopore reveals a significant phase shift of over 5 radians within a subnanometer distance. To better visualize the phase changes within the nanopore, an amplified phase image (5×) is depicted in Fig. 3(b). The spacing between contour lines corresponds to a 0.4π phase shift. The high-density contour lines within the nanopore indicate a rapid drop of Coulomb potential, signifying a strong electrostatic field in that area. The measured phase shift φ is related to the 3D potential distributions $V(x, y, z)$ as follows:

$$\varphi = C_E \int V(x, y, z)dz, \tag{1}$$

where C_E is the interaction constant and $C_E = 0.006\,526\,\mathrm{V}^{-1}\,\mathrm{nm}^{-1}$ for 300 keV electrons. Using Eq. (1), the projected Coulomb potential of the nanopore [shown as color maps in Fig. 3(c)] can be calculated from the phase image. A differential operation was further performed on the projected potential to obtain a projected electric field mapping. The strength and direction of the projected electric field are indicated by the white arrows in Fig. 3(c). Assuming that the electric field strength only varies in the x-y plane, the in-plane field strength can be obtained by dividing the projected electric field by the length of the pore. The resulting field strength is plotted in Fig. 3(d). The field strength within the nanopore reaches the order of 10 GV/m, which is extremely strong for an electrostatic field. The projected electric field distribution can also be observed in differential phase contrast (DPC) imaging in STEM mode. The DPC imaging of a similar nanopore, exhibiting comparable electric field distributions within the nanopore, is shown in Fig. S1 of the Supplemental Material [49].

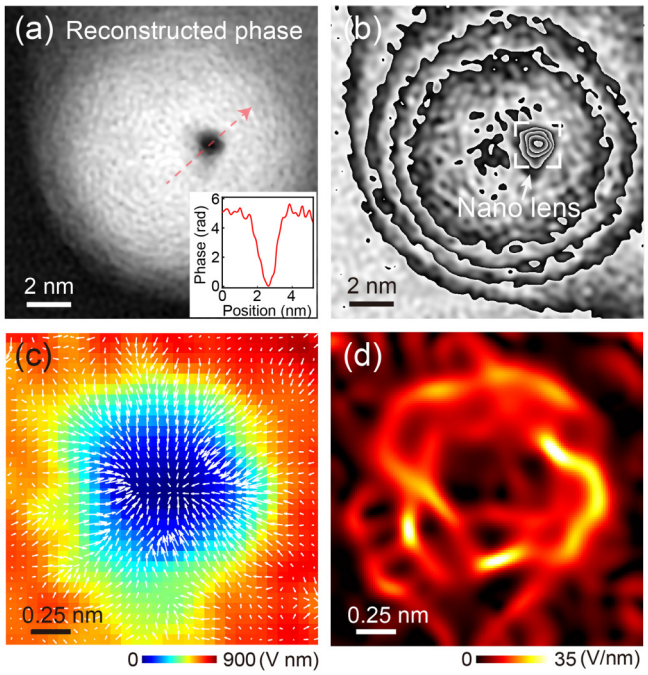

FIG. 3. Electric potential and electric field mapping of the nanopore lens. (a) Reconstructed phase image (unwrapped) of the electron exit wave from electron hologram. Inserted: phase line profile across the nanopore. (b) Amplified phase mapping (5×) of the nanopore and the surrounding area. The nanopore region shows high-density phase contour lines, marked by the white arrow. (c) Color-mapped projected potential and projected electric field (white arrows) of the nanopore lens. (d) Strength of the in-plane electric field inside the nanopore lens.

As shown in Fig. 3(c), the electric field points from the edge of the pore toward the center, causing the incident electron beam to deflect outward. The nanopore's deflection of negatively charged electrons is analogous to a deflection of light by a glass concave lens. To directly observe the modulating and lensing effect, we employed electron confocal imaging technique to image the changes in the probe when transmitting through the nanolens. Figure 4(a) shows the diagram of the electron confocal imaging setup [54–56].

A diffraction-limited electron probe was directed into the nanopore. The probe has a semiconvergent angle of 4.5 mrad, set by the probe-forming lens aperture. The effective lens aberrations within the aperture have been carefully tuned to zero using the probe corrector. The exit probe was then imaged through an aberration-corrected imaging system and recorded by a scintillator-based complementary metal-oxide semiconductor camera of the GIF system. The image of the probe in vacuum (far away from the sample) and the probe transmitting through the nanopore are compared in Figs. 4(d) and 4(e), respectively. Both images exhibit typical diffraction-limited Airy patterns, consisting of a bright intensity spot surrounded by a series of concentric rings with decreasing intensity. Significantly, the transmitted probe through the nanopore exhibits a brighter but smaller central spot surrounded by shrunken concentric rings.

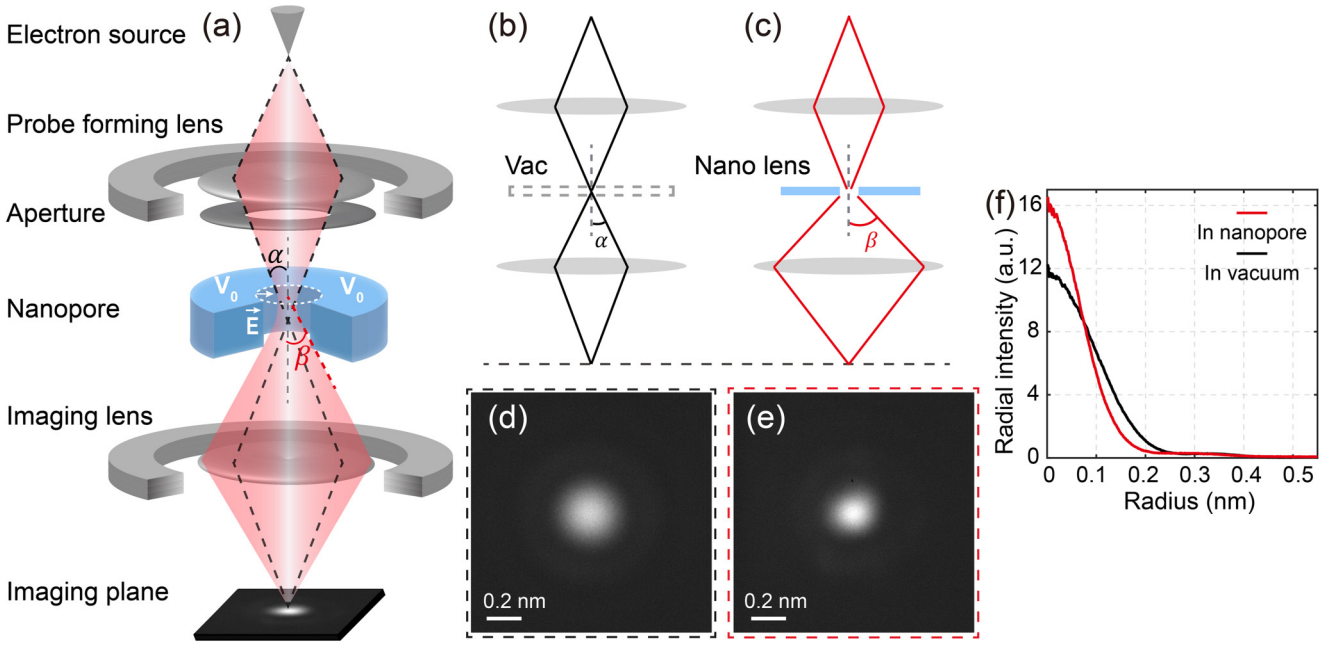

FIG. 4. Comparison of probe images when the probes transmit through vacuum and the nanopore lens. (a) Illustration of the electron confocal imaging mode to record the electron probe image on the detector plane. The simplified confocal optics are compared in panels (b) and (c). In panel (c), the effective convergent angle of the exit electron probe is increased due to the nanopore lens deflection. (d), (e) Experimental probe images (Airy patterns) on the detector plane: in vacuum and through the nano lens. (f) Radially integrated intensity line profiles from the center to the edge of the Airy patterns in panels (d) and (e).

Figure 4(f) compares the intensity line profiles across the center of two Airy patterns. When transmitted through the nanopore, the FWHM of the center spot intensity is reduced by 1.4 times compared to that of the probe image in vacuum. Meanwhile, the peak intensity increases by 1.3 times. This clearly demonstrates the deflection of incident high-energy electrons. Surprisingly, the nanopore functions as a concave lens, but the recorded Airy pattern shrinks. This is because Figs. 4(d) and 4(e) are magnified images of the electron probe transferring through the imaging lens system. Under the deflection of the outward field, the convergent angle of the exit probe increased when transmitting through the nanolens [illustrated in Figs. 4(b) and 4(c)]. The electron exit probe with an enlarged convergent angle formed a smaller Airy pattern in the final image plane, clearly indicating that the near-field Coulomb interaction provides a lensing effect for the matter wave of electrons. Figure S2 of the Supplemental Material [49] compares a series of probe images taken as the electron beam scanned over different regions (nanopore, carbon, and vacuum) on a similar sample.

We further performed an electron dynamical multislice simulation to confirm the changes in recorded probe images in confocal mode. Since a full three-dimensional atomic configuration of the nanopore is not experimentally accessible, we divided the experimental projected potential [Fig. 3(c)] into 345 layers, assuming that the Coulomb potential within the pore is uniformly distributed along the beam direction and only varies in the x-y plane. The total thickness of the structure is 69 nm, as previously measured with quantitative STEM. The incident probe's semiconvergent angle is 4.5 mrad, and the electron energy is 300 keV. Figure 5 compares the simulated probe intensities on the detector plane with a 3D surface rendering. In addition, Fig. 5(e) compares the intensity line profile across the centers of the Airy patterns. It evidences that a smaller but brighter Airy pattern is formed when the beam is transmitted through the nanolens, compared to that in vacuum. This aligns with the experimental results, which indicate that the effective convergent angle increases due to the deflection of the nanorange field as a concave lens.

The mean inner potential of amorphous carbon has been measured to be 10.8 V using electron holography. The potential difference between the matter and the vacuum energy level is then only in the order of 10 V. However, the potential drop within the nanopore is confined to a subnanometer range. This leads to an extremely high field strength in the order of 10 GV/m, which is 4 orders of magnitude higher than the breakdown field of the air. For comparison, the electric field in a conventional electrostatic lens in TEM is limited to the order of 10 MV/m to avoid high voltage breakdown [57]. The nanorange field strongly modulates the high-energy electrons, acting as a powerful electrostatic lens.

Following experimental mapping of the electric field within the nanopore and the direct observation of the associated defocusing lensing effect, we estimate the key optical parameter—the focal length of the electrostatic concave lens. In Fourier optics, the lens strength is determined by the phase modulation imposed on the incident wave. Thus, we derive the focal length from the measured phase shift $\phi(\rho)$ by off-axis electron holography, as shown in Fig. 3(b), where ρ denotes the radial coordinate. We fit the radial phase shift to a parabolic function $\phi(\rho) = a\rho^2$ (Fig. S3 of the Supplemental Material [49]), where the focal length f is related to a by

$$f = -\frac{k}{2a}. \tag{2}$$

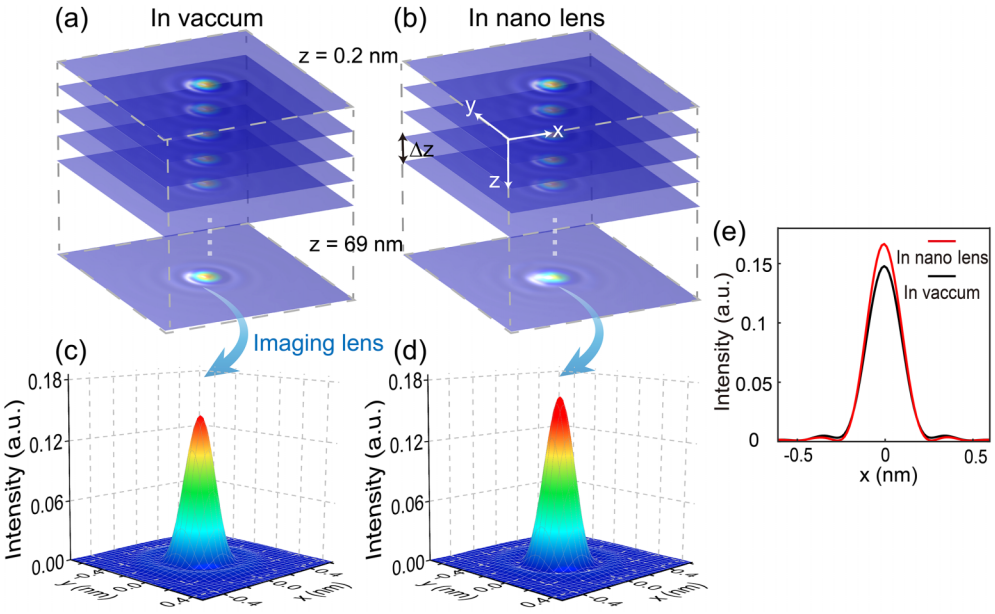

FIG. 5. Simulated electron probe intensities in confocal mode. (a) Probe intensity evolution when transmitting through vacuum and (b) through the nanopore lens. (c), (d) Corresponding intensity distributions at the detector plane after transferring through the imaging lens system. (e) Corresponding intensity line profiles across the center of the Airy patterns. Red: nanopore; blue: vacuum.

Here, k is the magnitude of the wave vector. For 300 keV electrons, $k = 3188\ \mathrm{nm}^{-1}$. Substituting the experimentally determined parameter ($a = 5.6\ \mathrm{nm}^{-2}$; see Fig. S3 of the Supplemental Material [49]) into Eq. (2) yields an effective focal length of $f \approx -285$ nm for the lens. The negative sign indicates that the nanopore acts as a defocusing (concave) lens for the incident high-energy electron beam. Remarkably, the focal length is on the order of only ~300 nm, reflecting an exceptionally strong lensing effect. In contrast, conventional magnetic lenses in TEM typically exhibit focal lengths of the order of millimeters. More generally, the focal length is governed by the curvature parameter a, indicating that it can, in principle, be tuned by adjusting the pore depth or radius, offering a route to engineered nanoscale electron optics. In addition, the imperfection of the nanopore structure induces some low-order nonrotation symmetric aberrations and leads to some distortions in the intensity of the probe image, as shown in Fig. 4(e). While the focal length is extremely short, the effect of the other high-order aberrations including the third-order spherical aberration can be neglected.

Based on Eq. (2), the influence of geometric size on the focal length can be analyzed. For a fixed nanopore diameter, the projected potential, and hence the accumulated phase shift, increases linearly with the length. Following $\phi(\rho) = a\rho^2$ and $f = -\frac{k}{2a}$, the coefficient a scales linearly with the length, while the focal length f is inversely proportional to it. Thus, increasing the nanopore length results in a stronger lensing, i.e., a shorter focal length.

Further, considering variations in the diameter, and under the approximation that the total projected phase shift remains constant, since $a_1{\rho_1}^2 = a_2{\rho_2}^2$ and correspondingly $\frac{f_2}{f_1} = \frac{a_1}{a_2} = (\frac{\rho_2}{\rho_1})^2$, the scaling relations indicate that the focal length f is proportional to the square of the diameter. Therefore, a larger diameter leads to weaker focusing and a longer focal length. However, this scaling breaks down for sufficiently large diameters. In this regime, the potential variation is significant only near the nanopore edge, while the central region exhibits an almost flat potential. Since this flat region contributes negligibly to the phase curvature, the effective lensing strength is significantly reduced.

III. DISCUSSIONS

Mityureva *et al.* proposed using a nanohole as a matter lens for atomic and molecular optics [58], extending Smirnov's concept of an atomic-scale corpuscular lens [59]. In this work, we show that a nano-object can indeed function as an electron lens for wave function modulation and lensing. Previous experiments and image simulations by Cowley, Smirnov, Dunin-Borkowski *et al.* have also demonstrated atomic focusers for high-energy electrons [60–64]. The Coulomb potential decreases quickly from the nuclei region to the outer shell, resulting in kilovolt changes over a sub-Angstrom length. This makes a single atom or a column of atoms a stronger electrostatic lens for electron lensing than the nanopore lens described in this work. However, controlling a single atom or a column of atoms to precisely focus an incident electron beam still poses a challenge, and the lensing effect may be influenced by nonboring atomic columns in crystal. In contrast, our approach employs a nanoscale structure to scatter and shape the electron beam. This enables substantially greater control over the relative positioning between the incident beam and the structure, which is not readily achievable in atomic focusing system.

More importantly, the nanopore structure considered here generates a potential gradient with a sign opposite to that of conventional atomic potentials. Consequently, it acts as a concave (defocusing) lens for high-energy electrons, in contrast to the convex (focusing) behavior associated with

atomic focusers. Achieving a concave lensing effect for high-energy electrons remains a significant challenge. According to Scherzer theorem [65], a concave lens for high-energy electrons cannot be realized using rotationally symmetric electromagnetic fields in vacuum, due to fundamental constraints imposed by the governing field equations. More specifically, the electromagnetic fields are static and rotationally symmetric, and no space charge is present. Under these conditions, electromagnetic lenses have positive spherical aberration (i.e., cannot be concave). In vacuum, the electrostatic potential satisfies Laplace's equation, which forbids local maxima or minima and requires the potential to be a harmonic function. The present structure, however, lies outside these constraints. By exploiting the inner potential of matter, the nanopore creates a non-charge-free electrostatic environment—one not subject to the conditions underlying Scherzer's theorem. As the electron beam traverses the nanopore, its wave function acquires a spatially varying phase shift determined by the local Coulomb potential of the nanostructure. This interaction effectively introduces a phase modulation that acts like a concave lens.

The nanomatter lens demonstrated here also has several limitations. The fixed geometry restricts the convergence angle of the incident beam, as larger angles would cause the beam to strike the inner walls of the pore. However, as in atomic electron lenses, such structures are not intended for primary focusing but for modulating an already focused electron beam in ways unattainable with conventional electromagnetic lenses. The nanomatter lens is also not tunable and thus acts as a static electron-optical element, and the long-term stability and radiation tolerance may be limited in the present implementation. However, the primary aim is not to realize a fully functional and tunable electron-optical component, but rather to demonstrate a physical mechanism—the concave lensing of high-energy electrons by the inner potential of matter. This demonstration may inspire future developments of fully functional and tunable nanoscale electron lenses based on similar underlying principles. The long-term stability and radiation tolerance could also be improved by using metallic glasses instead of amorphous carbon.

IV. CONCLUSION

In conclusion, we have presented an experimental demonstration that the rapid changes of the Coulomb potential within a sub-nanometer pore in a solid can generate a strong electric field in the order of 10 GV/m, which effectively deflects the incident high-energy electrons as a strong electron concave matter lens. This provides an alternation for conventional electromagnetic lensing and extends electron manipulation and lensing to nanoscale electron optics.

ACKNOWLEDGMENTS

This work was supported by the National Natural Science Foundation of China (Grant No. 62171136) and Quantum Science and Technology—National Science and Technology Major Project (Grant No. 2024ZD0300103).

DATA AVAILABILITY

The data that support the findings of this study are available from the corresponding author upon reasonable request.

[1] K. W. Urban, Studying atomic structures by aberration-corrected transmission electron microscopy, Science **321**, 506 (2008).

[2] S. J. Pennycook, The impact of STEM aberration correction on materials science, Ultramicroscopy **180**, 22 (2017).

[3] D. A. Muller, L. F. Kourkoutis, M. Murfitt, J. H. Song, H. Y. Hwang, J. Silcox, N. Dellby, and O. L. Krivanek, Atomic-scale chemical imaging of composition and bonding by aberration-corrected microscopy, Science **319**, 1073 (2008).

[4] P. D. Nellist, M. F. Chisholm, N. Dellby, O. L. Krivanek, M. F. Murfitt, Z. S. Szilagyi, A. R. Lupini, A. Borisevich, W. H. Sides, and S. J. Pennycook, Direct sub-angstrom imaging of a crystal lattice, Science **305**, 1741 (2004).

[5] B. E. Warren, *X-ray Diffraction* (Dover Publications, New York, 1990).

[6] A. T. Boothroyd, *Principles of Neutron Scattering from Condensed Matter*, 1st ed. (Oxford University Press, New York, 2020).

[7] P. W. Hawkes and E. Kasper, *Principles of Electron Optics*, 2nd ed. (Elsevier/AP, Academic Press, an imprint of Elsevier, London, 2018).

[8] R. Erni, M. D. Rossell, C. Kisielowski, and U. Dahmen, Atomic-resolution imaging with a sub-50-pm electron probe, Phys. Rev. Lett. **102**, 096101 (2009).

[9] H. Sawada, N. Shimura, F. Hosokawa, N. Shibata, and Y. Ikuhara, Resolving 45-pm-separated Si-Si atomic columns with an aberration-corrected STEM, Microscopy **64**, 213 (2015).

[10] L. H. G. Tizei, R. Nakanishi, R. Kitaura, H. Shinohara, and K. Suenaga, Core-level spectroscopy to probe the oxidation state of single europium atoms, Phys. Rev. Lett. **114**, 197602 (2015).

[11] M. Q. Xu, A. W. Li, M. Gao, and W. Zhou, Single-atom electron microscopy for energy-related nanomaterials, J. Mater. Chem. A **8**, 16142 (2020).

[12] F. S. Hage, G. Radtke, D. M. Kepaptsoglou, M. Lazzeri, and Q. M. Ramasse, Single-atom vibrational spectroscopy in the scanning transmission electron microscope, Science **367**, 1124 (2020).

[13] N. Shibata, S. D. Findlay, Y. Kohno, H. Sawada, Y. Kondo, and Y. Ikuhara, Differential phase-contrast microscopy at atomic resolution, Nat. Phys. **8**, 611 (2012).

[14] K. Müller, F. F. Krause, A. Béché, M. Schowalter, V. Galioit, S. Löffler, J. Verbeeck, J. Zweck, P. Schattschneider, and A. Rosenauer, Atomic electric fields revealed by a quantum mechanical approach to electron picodiffraction, Nat. Commun. **5**, 5653 (2014).

[15] N. Shibata, T. Seki, G. Sánchez-Santolino, S. D. Findlay, Y. Kohno, T. Matsumoto, R. Ishikawa, and Y. Ikuhara, Electric field imaging of single atoms, Nat. Commun. **8**, 15631 (2017).

[16] W. P. Gao, C. Addiego, H. Wang, X. X. Yan, Y. S. Hou, D. X. Ji, C. Heikes, Y. Zhang, L. Z. Li, H. X. Huyan, T. Blum, T. Aoki, Y. F. Nie, D. G. Schlom, R. Q. Wu, and X. Q. Pan, Real-space charge-density imaging with sub-angstrom resolution by four-dimensional electron microscopy, Nature (London) **575**, 480 (2019).

[17] Q. Zheng, T. L. Feng, J. A. Hachtel, R. Ishikawa, Y. Q. Cheng, L. Daemen, J. Xing, J. C. Idrobo, J. Q. Yan, N. Shibata, Y. Ikuhara, B. C. Sales, S. T. Pantelides, and M. F. Chi, Direct visualization of anionic electrons in an electride reveals inhomogeneities, Sci. Adv. **7**, eabe6819 (2021).

[18] Y. Kohno, T. Seki, S. D. Findlay, Y. Ikuhara, and N. Shibata, Real-space visualization of intrinsic magnetic fields of an antiferromagnet, Nature (London) **602**, 234 (2022).

[19] M. Haider, S. Uhlemann, E. Schwan, H. Rose, B. Kabius, and K. Urban, Electron microscopy image enhanced, Nature (London) **392**, 768 (1998).

[20] O. L. Krivanek, N. Dellby, and A. R. Lupini, Towards sub-Å electron beams, Ultramicroscopy **78**, 1 (1999).

[21] H. Müller, S. Uhlemann, P. Hartel, and M. Haider, Advancing the hexapole C_s-corrector for the scanning transmission electron microscope, Microsc. Microanal. **12**, 442 (2006).

[22] E. Ruska, The development of the electron-microscope and of electron-microscopy, Rev. Mod. Phys. **59**, 627 (1987).

[23] P. W. Hawkes, *Magnetic Electron Lenses*, *Topics in Current Physics* (Springer, Berlin and New York, 1982), Vol. 18.

[24] O. L. Krivanek, N. Dellby, R. J. Keyse, M. F. Murfitt, C. S. Own, and Z. S. Szilagyi, Advances in aberration-corrected scanning transmission electron microscopy and electron energy-loss spectroscopy, Adv. Imaging Electron Phys. **153**, 121 (2008).

[25] M. Haider, P. Hartel, H. Müller, S. Uhlemann, and J. Zach, Current and future aberration correctors for the improvement of resolution in electron microscopy, Phil. Trans. R. Soc. A **367**, 3665 (2009).

[26] J. van Tilborg, S. Steinke, C. G. R. Geddes, N. H. Matlis, B. H. Shaw, A. J. Gonsalves, J. V. Huijts, K. Nakamura, J. Daniels, C. B. Schroeder, C. Benedetti, E. Esarey, S. S. Bulanov, N. A. Bobrova, P. V. Sasorov, and W. P. Leemans, Active plasma lensing for relativistic laser-plasma-accelerated electron beams, Phys. Rev. Lett. **115**, 184802 (2015).

[27] S. Kuschel, D. Hollatz, T. Heinemann, O. Karger, M. B. Schwab, D. Ullmann, A. Knetsch, A. Seidel, C. Rödel, M. Yeung, M. Leier, A. Blinne, H. Ding, T. Kurz, D. J. Corvan, A. Sävert, S. Karsch, M. C. Kaluza, B. Hidding, and M. Zepf, Demonstration of passive plasma lensing of a laser wakefield accelerated electron bunch, Phys. Rev. Accel. Beams **19**, 071301 (2016).

[28] E. Jones, M. Becker, J. Luiten, and H. Batelaan, Laser control of electron matter waves, Laser Photon. Rev. **10**, 214 (2016).

[29] F. J. G. de Abajo and A. Konecná, Optical modulation of electron beams in free space, Phys. Rev. Lett. **126**, 123901 (2021).

[30] M. C. C. Mihaila, P. Weber, M. Schneller, L. Grandits, S. Nimmrichter, and T. Juffmann, Transverse electron-beam shaping with light, Phys. Rev. X **12**, 031043 (2022).

[31] O. Schwartz, J. J. Axelrod, S. L. Campbell, C. Turnbaugh, R. M. Glaeser, and H. Müller, Laser phase plate for transmission electron microscopy, Nat. Methods **16**, 1016 (2019).

[32] Y. Uesugi, Y. Kozawa, and S. Sato, Properties of electron lenses produced by ponderomotive potential with Bessel and Laguerre-Gaussian beams, J. Opt. **24**, 054013 (2022).

[33] D. S. Black, K. J. Leedle, Y. Miao, U. Niedermayer, R. L. Byer, O. Solgaard, and A. Collaboration, Laser-driven electron lensing in silicon microstructures, Phys. Rev. Lett. **122**, 104801 (2019).

[34] H. Boersch, Über die kontraste von atomen im elektronenmikroskop, Z. Naturforsch. A **2**, 615 (1947).

[35] K. Schultheiss, F. Pérez-Willard, B. Barton, D. Gerthsen, and R. R. Schröder, Fabrication of a Boersch phase plate for phase contrast imaging in a transmission electron microscope, Rev. Sci. Instrum. **77**, 033701 (2006).

[36] C. J. Edgcombe, Imaging by Zernike phase plates in the TEM, Ultramicroscopy **167**, 57 (2016).

[37] R. Danev, B. Buijsse, M. Khoshouei, J. M. Plitzko, and W. Baumeister, Volta potential phase plate for in-focus phase contrast transmission electron microscopy, Proc. Nat. Acad. Sci. USA **111**, 15635 (2014).

[38] A. H. Tavabi, M. Beleggia, V. Migunov, A. Savenko, O. Öktem, R. E. Dunin-Borkowski, and G. Pozzi, Tunable Ampere phase plate for low dose imaging of biomolecular complexes, Sci. Rep. **8**, 5592 (2018).

[39] R. Shiloh, Y. Lereah, Y. Lilach, and A. Arie, Sculpturing the electron wave function using nanoscale phase masks, Ultramicroscopy **144**, 26 (2014).

[40] R. Shiloh, P. H. Lu, R. Remez, A. H. Tavabi, G. Pozzi, R. E. Dunin-Borkowski, and A. Arie, Nanostructuring of electron beams, Phys. Scr. **94**, 034004 (2019).

[41] D. Roitman, R. Shiloh, P. H. Lu, R. E. Dunin-Borkowski, and A. Arie, Shaping of electron beams using sculpted thin films, ACS Photon. **8**, 3394 (2021).

[42] V. Grillo, A. H. Tavabi, E. Yucelen, P. H. Lu, F. Venturi, H. Larocque, L. Jin, A. Savenko, G. C. Gazzadi, R. Balboni, S. Frabboni, P. Tiemeijer, R. E. Dunin-Borkowski, and E. Karimi, Towards a holographic approach to spherical aberration correction in scanning transmission electron microscopy, Opt. Express **25**, 21851 (2017).

[43] R. Shiloh, R. Remez, P. H. Lu, L. Jin, Y. Lereah, A. H. Tavabi, R. E. Dunin-Borkowski, and A. Arie, Spherical aberration correction in a scanning transmission electron microscope using a sculpted thin film, Ultramicroscopy **189**, 46 (2018).

[44] A. Béché, R. Van Boxem, G. Van Tendeloo, and J. Verbeeck, Magnetic monopole field exposed by electrons, Nat. Phys. **10**, 26 (2014).

[45] J. Verbeeck, A. Beche, K. Muller-Caspary, G. Guzzinati, M. A. Luong, and M. Den Hertog, Demonstration of a 2 × 2 programmable phase plate for electrons, Ultramicroscopy **190**, 58 (2018).

[46] C. L. Zheng, T. C. Petersen, H. Kirmse, W. Neumann, M. J. Morgan, and J. Etheridge, Axicon lens for electrons using a magnetic vortex: The efficient generation of a Bessel beam, Phys. Rev. Lett. **119**, 174801 (2017).

[47] V. Grillo, E. Karimi, G. C. Gazzadi, S. Frabboni, M. R. Dennis, and R. W. Boyd, Generation of nondiffracting electron Bessel beams, Phys. Rev. X **4**, 011013 (2014).

[48] A. M. Blackburn and J. C. Loudon, Vortex beam production and contrast enhancement from a magnetic spiral phase plate, Ultramicroscopy **136**, 127 (2014).

[49] See Supplemental Material at http://link.aps.org/supplemental/10.1103/2mgp-xgv1 for details on amorphous carbon preparation, DPC imaging of the nanopore lens, scanning confocal

probe images, and the parabolic phase modulation imparted to the incident beam by the nano lens.

[50] J. M. LeBeau, S. D. Findlay, L. J. Allen, and S. Stemmer, Quantitative atomic resolution scanning transmission electron microscopy, Phys. Rev. Lett. **100**, 206101 (2008).

[51] A. Rosenauer, T. Mehrtens, K. Müller, K. Gries, M. Schowalter, P. V. Satyam, S. Bley, C. Tessarek, D. Hommel, K. Sebald, M. Seyfried, J. Gutowski, A. Avramescu, K. Engl, and S. Lutgen, Composition mapping in InGaN by scanning transmission electron microscopy, Ultramicroscopy **111**, 1316 (2011).

[52] C. Dwyer, C. Maunders, C. L. Zheng, M. Weyland, P. C. Tiemeijer, and J. Etheridge, Sub-0.1 nm-resolution quantitative scanning transmission electron microscopy without adjustable parameters, Appl. Phys. Lett. **100**, 191915 (2012).

[53] H. Kauko, C. L. Zheng, Y. Zhu, S. Glanvill, C. Dwyer, A. M. Munshi, B. O. Fimland, A. T. J. van Helvoort, and J. Etheridge, Compositional analysis of GaAs/AlGaAs heterostructures using quantitative scanning transmission electron microscopy, Appl. Phys. Lett. **103**, 232111 (2013).

[54] P. Wang, G. Behan, M. Takeguchi, A. Hashimoto, K. Mitsuishi, M. Shimojo, A. I. Kirkland, and P. D. Nellist, Nanoscale energy-filtered scanning confocal electron microscopy using a double-aberration-corrected transmission electron microscope, Phys. Rev. Lett. **104**, 200801 (2010).

[55] J. Etheridge, S. Lazar, C. Dwyer, and G. A. Botton, Imaging high-energy electrons propagating in a crystal, Phys. Rev. Lett. **106**, 160802 (2011).

[56] C. L. Zheng, Y. Zhu, S. Lazar, and J. Etheridge, Fast imaging with inelastically scattered electrons by off-axis chromatic confocal electron microscopy, Phys. Rev. Lett. **112**, 166101 (2014).

[57] B. Lencová, Electrostatic lenses, in *Handbook of Charged Particle Optics*, edited by J. Orloff, 2nd ed. (CRC Press/Taylor & Francis, Boca Raton, 2009), p. 161.

[58] A. A. Mityureva, V. V. Smirnov, and O. A. Vorobiev, A nanohole as an atomic lens for atoms and molecules, J. Phys. D: Appl. Phys. **34**, L65 (2001).

[59] V. V. Smirnov, Atomic focusers, J. Phys. D: Appl. Phys. **31**, 1548 (1998).

[60] J. M. Cowley, J. C. H. Spence, and V. V. Smirnov, The enhancement of electron microscope resolution by use of atomic focusers, Ultramicroscopy **68**, 135 (1997).

[61] J. M. Cowley, R. E. Dunin-Borkowski, and M. Hayward, The contrast of images formed by atomic focusers, Ultramicroscopy **72**, 223 (1998).

[62] J. M. Cowley, Electron holography with atomic focusers, Phys. Rev. Lett. **84**, 3618 (2000).

[63] R. E. Dunin-Borkowski and J. M. Cowley, Simulations for imaging with atomic focusers, Acta Crystal. A **55**, 119 (1999).

[64] V. V. Smirnov and J. M. Cowley, In-line electron holography with an atomic focuser source, Phys. Rev. B **65**, 064109 (2002).

[65] O. Scherzer, Über einige fehler von elektronenlinsen, Z. Angew. Phys. **101**, 593 (1936).